Dynamics of Vertical Magnetic Suspension Rotor and Touchdown Bearing: Touchdown Mechanism

Zilin Li[1], Congtao Wang[2], Zixi Wang[1*] and Yuming Wang[1]
[1] State Key Laboratory of Tribology, Department of Mechanical Engineering, Tsinghua University, Beijing 100084, Beijing, China;
[2] Shenyang University of Technology, Shenyang 110003, Liaoning, China.

Abstract

During touchdowns of active magnetic bearings (AMB), rotor will generate different trajectory on touchdown bearings (TDB). The full rub will cause violent collisions and damages to both parts. By modeling radial and axial contact between rotor and TDBs, the dynamic and thermodynamic touchdown model of a vertical rotor with internal TDBs were established. Numerical simulation showed that the orbit response of vertical rotor after touchdowns was forward whirl, which is divided into two states: dry-friction whirl and dry-friction whip. There's a limit speed associated with the natural frequency that enables the rotor to convert from synchronous positive precession to sub-synchronous positive precession. The contact force and temperature of inner race has increased significantly when rotor entering the sub-synchronous forward precession.

Keywords: Touchdown Bearing; Vertical Rotor; Dynamic Model; Forward whirl.

1 Introduction

Once the Active Magnetic Bearing (AMB) is powered off or overloaded, the rotor will fall and rub against the touchdown bearings (TDB). The function of TDB is to limit the maximum radial and axial displacement of the rotor, to avoid the collision and damage of the main parts of AMB. But in fact, TDB itself is a part that is prone to damage. A number of theoretical and experimental studies have found that severe damage often occurs on TDB, so fatigue failure isn't the main cause of TDB failure. At present, there's no effective life evaluation system for TDB, which has become a key factor restricting the development of AMB. (Schweitzer Kuesnacht (Switzerland)] & Maslen Charlottesville, VA (United States). Dept. Mechanical and Aerospace Engineering], 2009)

* Corresponding authors: Tel: 86 10 62794845; Email: zxwang@mail.tsinghua.edu.cn (Zixi Wang).

The initial states such as rotor imbalance (Hawkins et al., 2006), surface friction coefficient (Sun et al., 2004), material pairing (Zhu, 2010), and assembly error (Kärkkäinen et al., 2008), etc., will have a significant impact on the rotor dynamic behavior of the touchdown. In severe cases, the rotor and TDB will vibrate violently and cause damage to TDB. According to ISO 14839, three typical orbit responses (pendulum vibration, combined rub and bouncing, and full rub) can be detected in touchdown events. (ISO, 2012) Lyu Mindong established a touchdown trajectory response identification method for online monitoring and resuspension of the rotor touchdown. (Lyu et al., 2018) In different touchdown trajectories, the whirl of the rotor (shown as full rub) was prone to significantly higher contact force and heat than other states, which is one of the main reasons for the failure of TDB. (Zhu et al., 2018) Zhao Yulan established a multi-degree-of-freedom rigid rotor drop model, based on the nonlinear Hertzian contact and collision theory, which can effectively simulate the movement, force and heating of the rotor touchdown. (Zhao et al., 2015) Helfert built an AMB-rotor touchdown test bench, using a high-speed camera to capture the displacement, speed and acceleration of the rotor, inner ring, and rolling elements after the fall. (Helfert et al., 2006)

In the study of rotor dynamic, 'whirl' generally refers to the orbital movement of the eccentric mass of the rotor around the axis, mainly for the contact between the flexible rotor and the stator. Literature (Jacquet-Richardet et al., 2013) provides a literature review on this topic. According to the direction of the frictional force, the rotor presents a backward whirl state during the contact. Wilkes (J. C. Wilkes et al., 2010) divides the contact form into the following two categories:

- Dry-friction whirl. The rotor rolls on the surface of the stator without sliding, and the precession frequency is governed by the radius-to-clearance ratio at the contact position;
- Dry-friction whip. The rotor continuously slides on the surface of the stator, and the precession frequency is governed by the combined natural frequency of the connected rotor-stator system.

Although the touchdown of AMB rotor is similar to the traditional rotor rubbing, touchdown rubbing has characteristics such as mainly occurs in the inner ring of the bearing, rotatabel bearing support, and not distinguished rotor mode. Therefore, the touchdown dynamic behavior is very different from the traditional rotor rubbing.

When the vertical rotor drops, it first collides and rubs with the axial end surface of the stationary TDB inner ring. The inner ring accelerates to the rotor speed in a short time. Then the rotor will continue colliding and rolling in the radial gap. Since there is no radial constraint, the rotor will always be in full rub state. The direction of the friction force indicates that the rotor will form forward whirl during vertical rotor drops. In a vertical rotor drop test, Caprio found that the forward whirl speed of the rotor monotonously increased with the rotor speed at a low rotation speed, but the whirl speed no longer increased when the speed was higher than 2000r/min. (Caprio et al., 2004) Wilkes verified this phenomenon through a numerical model in a subsequent study, and proved that the aforementioned dry-friction whirl and dry-friction whip states also occurred in the vertical rotor forward whirl. (J. Wilkes et al., 2014) There is a combined natural frequency between two state transitions.

The current dry-friction whirl/whip research of vertical rotor touchdown still stays in the rotor trajectory, motion and related vibration frequency. Researchers generally pay more attention to the behavior of the rotor, and there is still a lack of related research on TDB. For the design of the AMB-rotor system especially TDB, more parameterized, detailed and specific calculation are needed. Therefore, this research focuses on the establishment of system touchdown dynamics and thermodynamic models to quantify the force and temperature characteristics of TDB. By improving and supplementing the existing theoretical system, it provides parameter optimization for the overall structure of the preliminary designed protective bearing. In the future, we will also verify our model through experiments.

2 Model

2.1 AMB-rotor-TDB test system

The AMB-rotor-TDB test system consists of a rotor, 2 groups of radial and 1 group of axial AMBs and 2 groups of TDBs (Figure 1). The upper TDB bears the axial and radial load of the rotor, and the lower TDB only bears the radial load of the rotor. See Table 1 for relevant structural parameters of the rotor and bearing system. Use hybrid ceramic ball bearings as TDB solution. At each side of the rotor, a pair of 71938AC angular contact ball bearings are installed, and they are installed face to face. The inner and outer rings of the bearing are made of GCr15(SAE 52100) bearing steel, and the rolling elements are made of Si_3N_4 ceramic balls. The mechanical and thermal parameters related to materials are shown in Table 2.

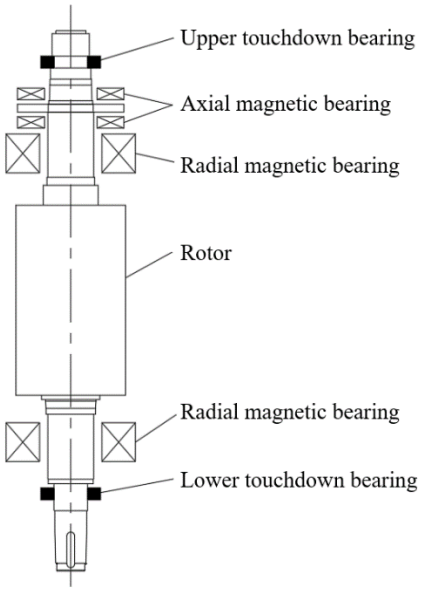

Figure 1: Schematic diagram of AMB-rotor-TDB system.

Rotor parameters	Value	TDB parameters	Value
Mass, kg	3000	Inner ring mass, kg	1.19
Length, mm	3054	Outer ring mass, kg	1.52
Momentum of Inertia, kg·m^2	130	Inner ring diameter, mm	190
Dynamic balance quality level	G6.3	Outer ring diameter, mm	260
Eccentricity, mm	0.02	Bearing width, mm	33
Radial clearance, mm	0.3	Bearing internal COF	0.0018
Axial clearance, mm	0.3	COF between rotor and inner ring	0.15

Table 1: AMB system parameters. (COF: Coefficient of friction)

Material parameters	Bearing steel GCr15	Ceramic ball Si3N4	Rotor Carbon steel
Elastic Modulus, GPa	219	310	210
Poisson's ratio	0.3	0.269	0.31
Thermal conductivity, W/(m·K)	40	3.5	50
Specific heat capacity, J/(kg·K)	450	800	480

Table 2: Material mechanics and thermal performance parameters.

2.2 Dynamic model of rotor-TDB system

When rotor dropped, considering the dynamic behavior of the upper TDB, the contact between rotor and TDB was divided into two parts: the axial end face and the radial inner face. Rotor first collided with the annular end surface of the inner ring. And then contacts and whirls in radial clearance. The contact and collision generated support force, friction force and friction torque. The system dynamics model of rotor-TDB and support base was shown in Figure 2.

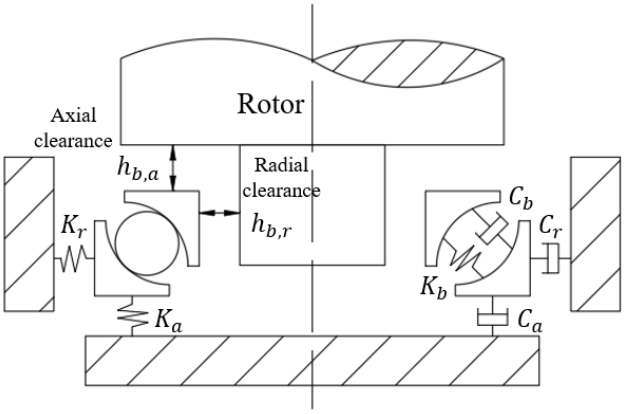

Figure 2: Rotor-TDB-support base system model.

$h_{b,a}, h_{b,r}$ represented the axial and radial drop clearances between the rotor and TDB respectively. K_b, C_b represented the stiffness and damping inside TDB. K_a, C_a represented the axial stiffness and damping between the outer ring of TDB and the support seat. K_r, C_r represented the radial stiffness and damping between the outer ring of TDB and the support seat.

The contact force between the rotor and TDB was calculated using the Hunt-Crossly collision model (Hunt & Crossley, 1975), which can calculate the impact of touchdown accurately. The calculation formula is:

$$F = \begin{cases} K\delta^n(1 + 1.5\kappa\dot{\delta}), & \delta > 0 \\ 0, & \delta \le 0 \end{cases}$$

δ was the amount of penetration between two contact surfaces. n was the contact coefficient. The coefficient κ is distributed in the interval from 0.08 to 0.2. K was the contact stiffness.

The friction of the system was calculated using the Coulomb friction model, as shown in Figure 3. The formula for calculating the radial friction force was $F_t = \mu F_r$. For the friction of the end surface, the force and torque were obtained by integrating the contact surface. Establish the coordinate system Oij according to the relative position of the rotor and the inner ring, then the relative speed between the inner ring and the rotor at point A in Figure 3 can be expressed by the following formula:

$$\overrightarrow{v_{A,rb}}(r,\varphi) = \left[\dot{\rho} + \left(\dot{\theta}_r - \dot{\theta}_b\right) r \sin\varphi\right]\vec{\imath} + \left[\left(\dot{\alpha} - \dot{\theta}_r\right)\rho - \left(\dot{\theta}_r - \dot{\theta}_b\right) r \cos\varphi\right]\vec{\jmath}$$

$\dot{\theta}_r, \dot{\theta}_b$ represented the rotation speed of the rotor and TDB; $\dot{\alpha}$ represented the rotation speed of the geometric center of the rotor around the fixed coordinate system Oxy, that was, the whirl speed; ρ represented the distance between the geometric center of the rotor and the origin of the coordinate.

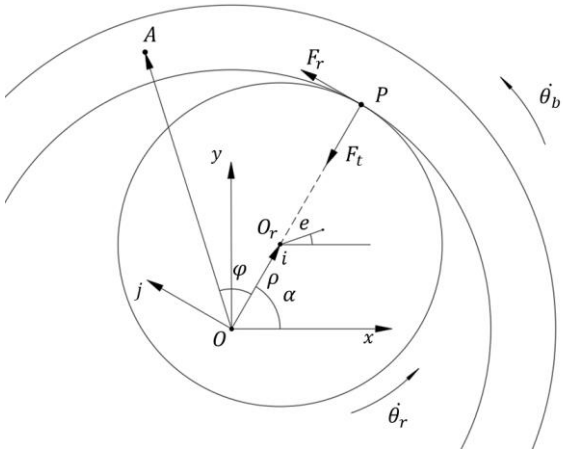

Figure 3: Model of friction force between rotor and TDB.

Approximately, the axial load can be regarded as uniformly distributed on the inner ring. Use P_a to represent the contact pressure of the end surface. The friction force on the entire surface can be calculated in two directions with the following formula:

$$F_{a,i} = -P_a\mu_f \cdot \int_{R_1}^{R_2}\int_{0}^{2\pi} \frac{\left[\dot{\rho} + \left(\dot{\theta}_r - \dot{\theta}_b\right) r \sin\varphi\right]\vec{\imath}}{\left\{\left[\dot{\rho} + \left(\dot{\theta}_r - \dot{\theta}_b\right) r \sin\varphi\right]^2 + \left[\left(\dot{\alpha} - \dot{\theta}_r\right)\rho - \left(\dot{\theta}_r - \dot{\theta}_b\right) r \cos\varphi\right]^2\right\}^{\frac{1}{2}}} r d\varphi dr$$

$$F_{a,j} = -P_a\mu_f \cdot \int_{R_1}^{R_2}\int_{0}^{2\pi} \frac{\left[\left(\dot{\alpha} - \dot{\theta}_r\right)\rho - \left(\dot{\theta}_r - \dot{\theta}_b\right) r \cos\varphi\right]\vec{\jmath}}{\left\{\left[\dot{\rho} + \left(\dot{\theta}_r - \dot{\theta}_b\right) r \sin\varphi\right]^2 + \left[\left(\dot{\alpha} - \dot{\theta}_r\right)\rho - \left(\dot{\theta}_r - \dot{\theta}_b\right) r \cos\varphi\right]^2\right\}^{\frac{1}{2}}} r d\varphi dr$$

The axial friction torque can also be obtained as:

$$T_a = \frac{2F_a\mu_f(R_2^3 - R_1^3)}{3(R_2^2 - R_1^2)}$$

R_1, R_2 represented the inner and outer radius of the end face of the bearing inner ring.

According to the Lagrange equation, the dynamic equations of the rotor drop in three directions during contact are established as follows:

$$m_r\left[\ddot{x_r} - e\sin(\theta_r)\,\ddot{\theta_r} - e\cos(\theta_r)\,\dot{\theta_r}^2\right] = -F_r\cos\alpha - F_t\sin\alpha$$

$$m_r\left[\ddot{y_r} + e\cos(\theta_r)\,\ddot{\theta_r} - e\sin(\theta_r)\,\dot{\theta_r}^2\right] = -F_r\sin\alpha + F_t\cos\alpha$$

$$m_r\ddot{z} = -m_r g + F_{a,z}$$

$$m_r e[-\sin(\theta_r)\,\ddot{x_r} + \cos(\theta_r)\,\ddot{y_r}] + (m_r e^2 + J_r)\ddot{\theta_r} = F_r e\sin(\alpha - \theta_r) - F_t e\cos(\alpha - \theta_r)$$

2.3 Thermodynamic model of rotor-TDB system

During the drop process of the rotor, the main heat sources considered come from three aspects: viscous friction torque, spin friction torque and contact load friction torque. Palmgren derives the friction torque inside the rolling bearing, and Harris further derives the spin torque of the rolling element relative to the inner ring and the outer ring. (Harris & Barnsby, 1998)The contact friction

torque can be directly calculated by the mechanical model. The total frictional heat generated by the final fall can be expressed as:

$$H_{total} = \sum \left(H_{i,e}^{j} + H_{r}^{j} + H_{a}^{j} \right)$$

$H_{i,e}$ was the friction heat generated by the rolling element with the inner and outer rings. H_r was the friction heat generated by the radial contact surface of the rotor and TDB. H_a was the friction heat generated by the axial end surface of the rotor and the upper TDB; the angle mark j indicated each pair of bearings.

Based on the theory of heat transfer, a one-dimensional heat transfer network model was established by calculating the heat transfer impedance of each component during the touchdown process of the rotor, considering the heat conduction and heat convection of the system (Figure 4). The heat transfer between the temperature nodes was expressed by the first-order differential equation as follows:

$$mC_p \Delta T = \Delta Q$$

m represented the mass, C_p represented the specific heat capacity, ΔT represented the temperature difference between the two temperature nodes. And Q represented the heat flux, R represented the thermal resistance of each part.

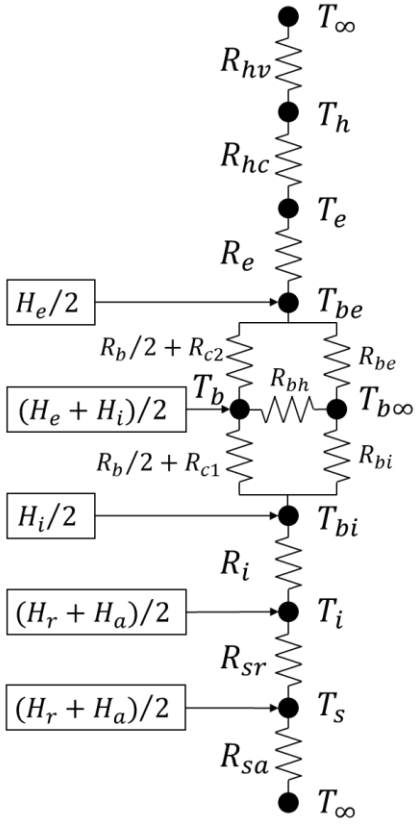

Figure 4: Schematic diagram of the heat transfer network of the rotor-TDB system.

Furthermore, each component of TDB will expand as the temperature rises. Considering the thermal expansion of the inner and outer rings and rolling elements, the thermally induced load inside TDB is:

$$F_{th} = K[\varepsilon_b + 0.5(\varepsilon_i - \varepsilon_e)\cos\alpha_0]^{3/2}$$

Among them, $\varepsilon_b, \varepsilon_i, \varepsilon_e$ respectively represented the expansion of the protective bearing rolling element, inner ring and outer ring. α_0 represented the initial contact angle.

3 Result

The model of the rotor-TDB system was established above, then the numerical simulation calculation was carried out. According to the speed target designing the test bench, two typical calculation examples were simulated. The initial speed was set to 3000 r/min and 6000 r/min. Suppose that the rotor lost AMB support and started to fall freely on the set speed at time 0. Figure 5 shows the operating conditions of the rotor touchdown event at an initial speed of 3000r/min within 1s, including axial displacement and contact force, radial touchdown trajectory, radial contact force, rotor and bearing speed, temperature of various parts, and temperature ascent rate of the inner ring.

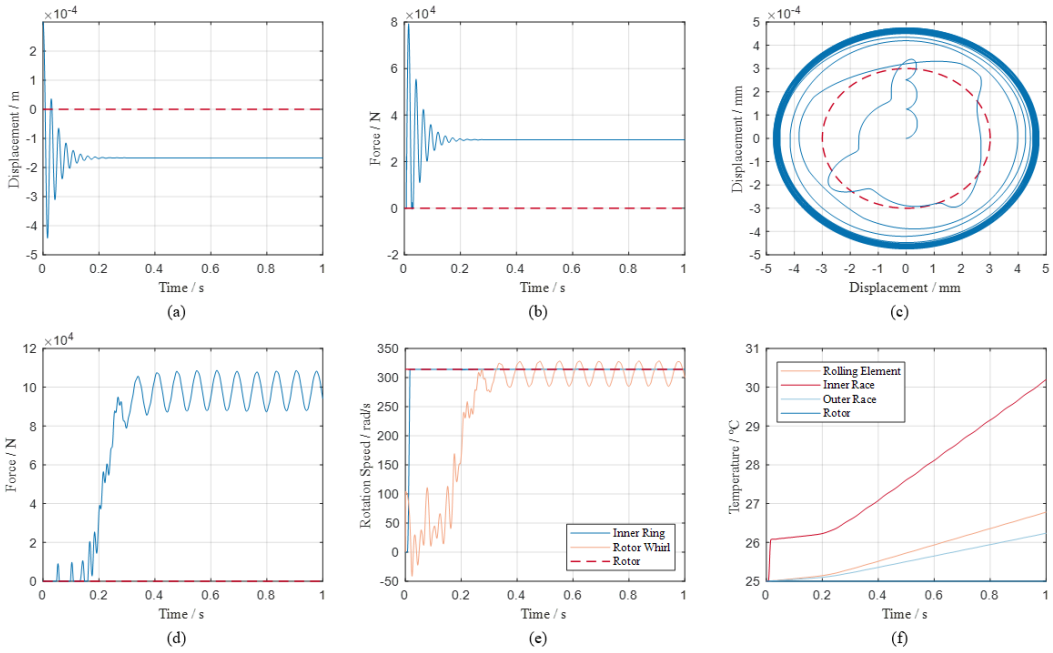

Figure 5: Numerical simulation results of rotor touchdown at 3000 r/min: (a) Rotor axial displacement; (b) Axial contact force of inner ring; (c) Rotor radial trajectory; (d) Radial contact force of inner ring; (e) Rotation speed; (f) System temperature change.

Numerical simulation results showed that, in the axial direction, the rotor reached a stable support state after several collisions and rebounds (Figure 5(a)). The maximum axial contact force occurred at the first collision (Figure 5(b)). The trajectory in the radial direction (Figure 5(c)) showed that the rotor entered a forward whirl state after several collisions, making an approximate circular motion. The radial contact force curve (Figure 5(d)) showed that the collision force was small in the first few collisions, then continued to rise after the rotor enters the forward whirl, finally fluctuated in a fixed interval. Figure 5(e) showed the change curve of the rotation speed of the rotor, the inner ring and the rotor whirl. It can be seen that during the initial axial contact between the rotor and inner ring, the

inner ring quickly accelerated to near the rotor speed and maintained a constant speed. The whirl speed of the rotor rose relatively slowly. It rose to the rotor speed as the rotor entered a forward whirl, and oscillated within a certain range. At this time, the rotor and the inner ring of TDB enter the synchronous positive precession state. Figure 5(f) showed the temperature changes of the various components of the system. The inner ring had a significant temperature increase during the first contact due to the rapid acceleration and collision friction in the axial direction. The temperature of other parts increased with time. The temperature rise of the rotor is not obvious due to its large mass. After the rotor enters the equilibrium state, the rate of temperature change was also balanced.

Change the initial drop speed to 6000 r/min for touchdown simulation. The partial results obtained were shown in Figure 6. It can be seen from this calculation that the whirl radius of the rotor trajectory increased (Figure 6(c)). The radial contact force was increased by 159.5% compared to 3000 r/min (Figure 6(d)). The whirl speed of the rotor did not rise to the rotor speed, but stabilized at about 400 rad/s (Figure 6(e)). The temperature of each part has a significant increase compared to the low speed (Figure 6(f)).

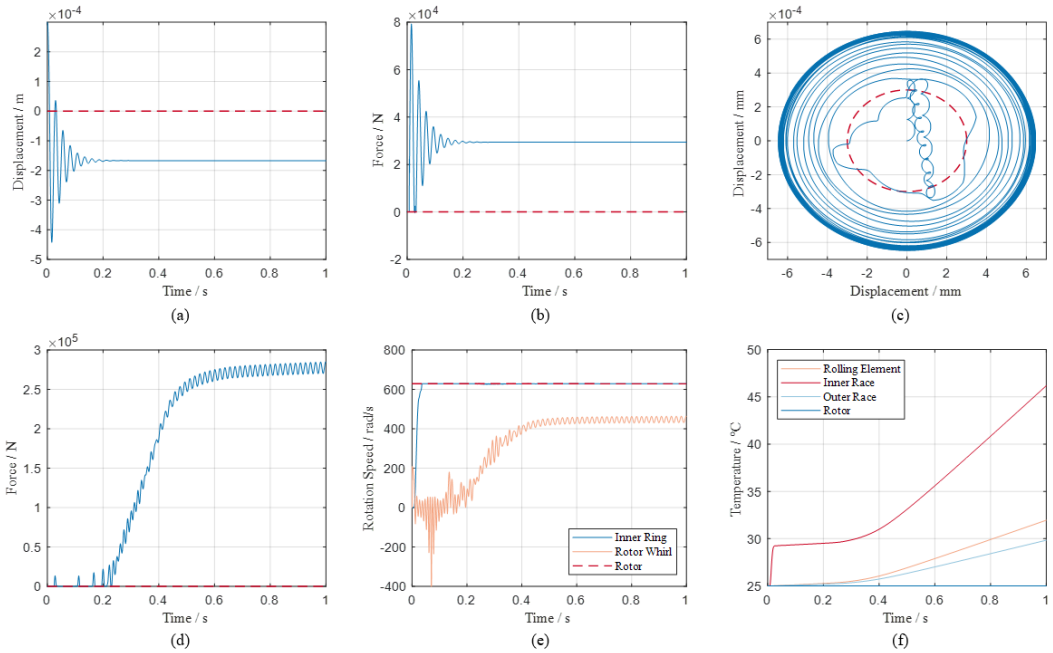

Figure 6: Numerical simulation results of rotor touchdown at 6000 r/min: (a) Rotor axial displacement; (b) Axial contact force of inner ring; (c) Rotor radial trajectory; (d) Radial contact force of inner ring; (e) Rotation speed; (f) System temperature change.

In order to study the relationship between the whirl speed and the rotor speed of vertical magnetic suspension rotor, a waterfall plot of the whirl speed distribution changing with the initial dropping speed was made, as shown in Figure 7. The X-axis represented the whirl speed, and the Y-axis represented the rotor rotation speed of the initial drop. When the rotor speed was lower than the limit speed (4000 r/min), the rotor forward whirl speed was equal to the rotor speed. The rotor and the inner ring underwent synchronous positive precession. At this time, the radial contact appeared as dry-friction whirl. When the rotor speed increased to 4000r/min or more, the rotor forward whirl speed became lower than the rotor speed. As the rotor speed increased, the difference between the rotor speed and the whirl speed increased. The rotor and the inner ring underwent sub-synchronous positive

precession. At this time, the form of radial contact was dry-friction whip. There was continuous sliding friction, causing more significant energy conversion and heating processes in the system.

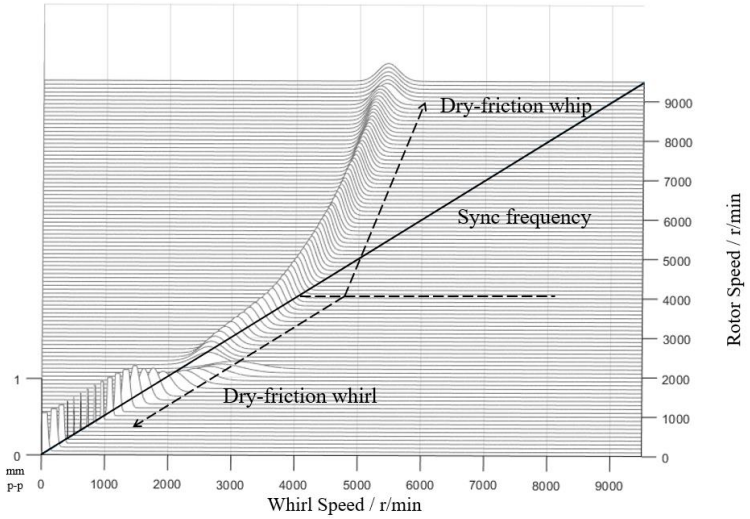

Figure 7: Waterfall plot of the rotor whirl speed at the upper TDB.

The above phenomenon was basically consistent with the rotor touchdown whirl phenomenon pointed out in the literature [14]. But it's worth noting that, literature [14] proposed that when the rotor speed exceeded the limit speed ω, the rotor whirl speed was equal to the limit speed ω. And our model observed that when the rotor speed exceeded the limit speed ω, the whirl speed was still increasing as the rotor speed increased. The differential speed between the rotor speed and the whirl speed also increased.

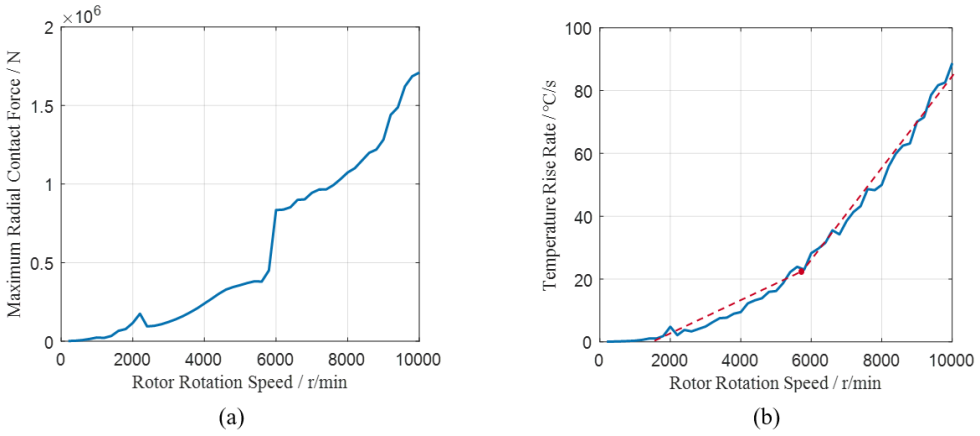

Figure 8: Change curve of (a) maximum radial contact force and (b) temperature rise rate.

Figure 8(a) plotted the change curve of the maximum radial contact force with the rotor speed when touchdown happened. It can be found that the maximum contact force increased monotonously with the increase of the speed. In addition, it's observed that around 6000 r/min, that is, when the increase in the whirl speed stopped, the contact force had a sudden increase. This was due to the rotor

form conversion of the synchronous positive precession to the sub-synchronous positive precession. The result was a significant increase in contact force and friction force. Figure 8(b) showed the change curve of the temperature rise rate of the inner ring with the speed, after the rotor entered the oscillation balance. It can also be found that the temperature rise rate increased with the rise of the speed. And after the rotor enters the sub-synchronous positive precession, the temperature rise slope increased obviously.

The above phenomenon can be summarized when the vertical rotor dropped on TDB, first axial collision was the most violent at the initial stage of the rotor drop. Its collision force was the largest. The radial collision force increased continuously until it enters the forward whirl. The forward whirl was divided into two states: dry-friction whirl and dry-friction whip. The two are distinguished by the rotor speed. At low speeds, it's dry-friction whirl, and at high speeds, dry-friction whip occurred. Monitoring the parameters can find that the latter brought greater radial contact force and more severe temperature rise to the rotor, both of which will have a significant impact on the stability and reliability of TDB, and then affect the life of TDB.

4 Discussion on the behavior of rotor whirl

In order to explain the dry-friction whirl and whip phenomena found in the rotor touchdown experiment by Caprio [13] and Wilkes [14], the difference in dynamic behavior between the two is derived from a theoretical perspective. When the inner ring is stationary at the beginning of the rotor drop, the axial touchdown will produce a large friction torque. Since the rotor mass is much larger than the bearing mass, the inner ring will quickly accelerate to the rotor speed $(\dot{\theta}_r \approx \dot{\theta}_b)$. For radial contact, the tangential velocity at point P (in Figure 3) on the rotor and bearing can be expressed by the following formula:

$$V_r = \rho \cdot \dot{\alpha} + R_r \cdot \dot{\theta}_r$$

$$V_b = R_1 \cdot \dot{\theta}_b$$

Among them, R_r represents the rotor radius and R_1 represents the inner radius of the bearing inner ring, $R_1 = R_r + h_{b,r}$. When the rotor is in contact with the inner ring, there is $\rho = h_{b,r}$. Therefore, $V_r < V_b$ in the initial stage of the fall, and the friction force direction is forward, relative to the direction of rotation. The rotor has a trend of forward whirl. The rotor is driven by the tangential friction F_t, which causes the whirl speed $\dot{\alpha}$ to increase continuously. Until $\dot{\alpha} = \dot{\theta}_r = \dot{\theta}_b$, there's $V_r = V_b$. At this time, the tangential friction force F_t at point P is 0, rotor and inner ring contact with dry-friction whirl. And the entire system reaches a balanced state.

However, as mentioned in literature [14], There is a limit rotation speed ω for the acceleration of $\dot{\alpha}$. When $\dot{\theta}_r$ is less than the limit speed ω, $\dot{\alpha}$ will take $\dot{\theta}_r$ as the equilibrium speed. When $\dot{\theta}_r$ is greater than ω, $\dot{\alpha}$ will use ω as the balance speed. At this time, the system will increase the penetration ρ between the rotor and inner ring to achieve balance, which will lead to an increase in contact force.

Then, according to different contact behaviors, the motion form of the rotor and the inner ring is defined as synchronous positive precession and sub-synchronous positive precession. The former corresponds to the dry-frictional whirl between the rotor and inner ring, indicated that the rotor speed $\dot{\theta}_r$ is equal to the whirl speed $\dot{\alpha}$. The latter corresponds to dry-friction whip, which means $\dot{\alpha} < \dot{\theta}_r$.

5 Conclusion

When the magnetic suspension rotor falls, it will have severe impact and rubbing on TDB. In this paper, a dynamic analysis of the vertical rotor touchdown process was carried out. By modeling the

contact of the axial end face, the inner ring radial direction and the rolling elements, a three-dimensional numerical simulation model of the dynamics and thermodynamics of the vertical rotor touchdown was established.

The movement mode of the vertical rotor after touchdown event was forward whirl. Under different working conditions, it can be divided into two states: dry-friction whirl and dry-friction whip. The former is synchronous positive precession, and the latter is sub-synchronous positive precession. There is a limit speed ω. When the rotor speed is lower than the limit speed, it falls into synchronous positive precession, the balance whirl speed is equal to the rotor speed. And when the rotor speed is higher than the limit speed, the rotor falls into sub-synchronous positive precession, the balance whirl speed is equal to the limit speed. The contact force and temperature between the rotor and TDB increased significantly since entering the sub-synchronous positive precession.

In the follow-up research, we will focus on the reasons for the sub-synchronous positive precession of the system, and investigate the influence of various parameters on the limiting speed that causes the whirl state to change. We are carrying out a drop test. In the future, the reliability of the rotor-TDB touchdown will be quantitatively evaluated from the perspective of system design.

References

Caprio, M. T., Murphy, B. T., & Herbst, J. D. (2004). Spin Commissioning and Drop Tests of a 130 kW-hr Composite Flywheel. *The 9th International Symposium on Magnetic Bearings*.

Harris, T. A., & Barnsby, R. M. (1998). Tribological Performance Prediction of Aircraft Gas Turbine Mainshaft Ball Bearings. *Tribology Transactions*, *41*(1), 60–68. https://doi.org/10.1080/10402009808983722

Hawkins, L., Filatov, A., Imani, S., & Prosser, D. (2006). Test Results and Analytical Predictions for Rotor Drop Testing of an Active Magnetic Bearing Expander/Generator. *Journal of Engineering for Gas Turbines and Power*, *129*(2), 522–529. https://doi.org/10.1115/1.2436549

Helfert, M., Ernst, M., Aeschlimann, B., & Nordmann, R. (2006). High-Speed Video Analysis of Rotor-Retainer-Bearing-Contacts Due to Failure of Active Magnetic Bearings. *10th International Symposium on Magnetic Bearings 2006*. http://tubiblio.ulb.tu-darmstadt.de/58906/

Hunt, K., & Crossley, E. (1975). Coefficient of restitution interpreted as damping in vibroimpact To cite this version : HAL Id : hal-01333795 Coefficient of Restitution Interpreted as Damping in Vibroimpact. *Journal of Applied Mechanics, American Society of Mechanical Engineers*, *42*, 440–445.

ISO. (2012). *ISO 14839-4 Mechanical Vibration - vibration of rotating machinery equipped with active magnetic bearings Part4: Technical guidelines*. https://www.iso.org/standard/50442.html

Jacquet-Richardet, G., Torkhani, M., Cartraud, P., Thouverez, F., Nouri Baranger, T., Herran, M., Gibert, C., Baguet, S., Almeida, P., & Peletan, L. (2013). Rotor to stator contacts in turbomachines. Review and application. *Mechanical Systems and Signal Processing*, *40*(2), 401–420. https://doi.org/10.1016/j.ymssp.2013.05.010

Kärkkäinen, A., Helfert, M., Aeschlimann, B., & Mikkola, A. (2008). Dynamic analysis of rotor system with misaligned retainer bearings. *Journal of Tribology*, *130*(2), 1–10. https://doi.org/10.1115/1.2908921

Lyu, M., Liu, T., Wang, Z., Yan, S., Jia, X., & Wang, Y. (2018). Orbit Response Recognition during Touchdowns by Instantaneous Frequency in Active Magnetic Bearings. *Journal of Vibration and Acoustics, Transactions of the ASME*, *140*(2), 1–11. https://doi.org/10.1115/1.4037850

Schweitzer Kuesnacht (Switzerland)], G. [Mechatronics C., & Maslen Charlottesville, VA (United States). Dept. Mechanical and Aerospace Engineering], E. H. [Virginia U. (2009). *Magnetic*

bearings. Theory, design, and application to rotating machinery. Springer, Berlin (Germany). https://doi.org/10.1007/978-3-642-00497-1

Sun, G., Palazzolo, A. B., Provenza, A., & Montague, G. (2004). Detailed ball bearing model for magnetic suspension auxiliary service. *Journal of Sound and Vibration*, *269*(3–5), 933–963. https://doi.org/10.1016/S0022-460X(03)00207-4

Wilkes, J. C., Childs, D. W., Dyck, B. J., & Phillips, S. G. (2010). The Numerical and Experimental Characteristics of Multimode Dry-Friction Whip and Whirl. *Journal of Engineering for Gas Turbines and Power*, *132*(5), 52503-1-52503–52509. https://doi.org/10.1115/1.3204658

Wilkes, J., Moore, J., Ransom, D., & Vannini, G. (2014). An improved catcher bearing model and an explanation of the forward whirl/whip phenomenon observed in active magnetic bearing transient drop experiments. *Journal of Engineering for Gas Turbines and Power*, *136*(4), 1–11. https://doi.org/10.1115/1.4025890

Zhao, Y., Yang, G., Shi, Z., & Zhao, L. (2015). Thermal Analysis and Simulation of Auxiliary Bearings and Its Application in the High Temperature Reactor-10. *Journal of Tribology*, *138*(1), 011102. https://doi.org/10.1115/1.4031003

Zhu, Z. Y., Mo, J. L., Wang, D. W., Zhao, J., Zhu, M. H., & Zhou, Z. R. (2018). Study on the Correlation Between Dynamical Behavior and Friction/Wear Mechanism Under the Effect of Grooves. *Journal of Materials Engineering and Performance*, *27*(6), 2875–2884. https://doi.org/10.1007/s11665-018-3373-z

ZHU C. (2010). Effect of backup bearing impact surface pairs on rotor dropping transient response after active magnetic bearing failure. *Journal of Vibration Engineering*, 23(05): 475-479. https://doi.org/10.16385/j.cnki.issn.1004-4523.2010.05.007